Volumetric Cerebral Perfusion Imaging in Healthy Adults: Regional Distribution, Laterality, and Repeatability of Pulsed Continuous Arterial Spin Labeling (PCASL)

Adolf Pfefferbaum[a,b], **Sandra Chanraud**[a,b], **Anne-Lise Pitel**[b], **Ajit Shankaranarayanan**[c], **David C. Alsop**[d], **Torsten Rohlfing**[a], and **Edith V. Sullivan**[b]

[a] Neuroscience Program, SRI International, Menlo Park, CA

[b] Department of Psychiatry & Behavioral Sciences, Stanford University School of Medicine, Stanford, CA

[c] MR Applied System Laboratory, GE Healthcare, Menlo Park, CA

[d] Department of Radiology, Beth Israel Deaconess Medical Center and Harvard Medical School, Boston, MA

Abstract

The regional distribution, laterality, and reliability of volumetric pulsed continuous arterial spin labeling (PCASL) measurements of cerebral blood flow (CBF) in cortical, subcortical, and cerebellar regions were determined in 10 normal volunteers studied on two occasions separated by 3 to 7 days. Regional CBF, normalized for global perfusion, was highly reliable when measured on separate days. Several regions showed significant lateral asymmetry; notably, in frontal regions CBF was greater in the right than left hemisphere, whereas left was greater than right in posterior regions. There was considerable regional variability across the brain, whereby the posterior cingulate and central and posterior precuneus cortices had the highest perfusion and the globus pallidus the lowest gray matter perfusion. The latter may be due to iron-induced T1 shortening affecting labeled spins and computed CBF signal. High CBF in the posterior cingulate and posterior and central precuneus cortices in this task-free acquisition suggests high activity in these principal nodes of the "default mode network."

Keywords

cerebral blood flow; CBF; precuneus; reliability; laterality; brain iron; MRI

1. Introduction

Cognitive, sensory, and motor functions are dependent on the health of the local blood perfusion in the brain. Many established approaches for measurement of regional cerebral blood flow (CBF) require the use of moderately invasive imaging methods (for review, Barbier, et al., 2001, Wintermark, et al., 2005), including Single Photon Emission Computed

Tomography (SPECT) or Positron Emission Tomography (PET), both requiring injection of radioactive tracer, x-ray CT with Xenon inhalation, or MRI methods requiring intravenous contrast agent injection. By contrast, the MRI method of Arterial Spin Labeling (ASL) enables measurement of cerebral perfusion without the need for exogenous tracers (Detre, et al., 1992). The approach magnetically inverts, or "labels," the nuclear magnetization of water molecules of flowing blood in a region proximal to the imaged volume. As the labeled spins enter the imaging slice, they exchange with tissue water spins and slightly attenuate the image signal. Subtraction of the image after labeling from an unlabeled reference image provides an estimate of the amount of blood that has flowed into the tissue (Alsop and Detre, 1996). Challenges to the technique include the low signal intensity differences (~1%), rapid T1 decay of the labeled spins, and uncertainty of the amount of time necessary for delivery to the image slice, i.e., the transit time, which may increase with advancing age (Campbell and Beaulieu, 2006).

A comparison of ASL, fMRI-derived hemodynamics, and $H_2{}^{15}O$ PET, which is considered a gold standard for CBF imaging (Carroll, et al., 2002), noted high correspondence among these three modalities based on the occipital gray matter samples examined. These data provided convergent validity for the use of any of these approaches in quantifying CBF despite lower signal-to-noise ratio (SNR) of ASL compared with PET (Ernst, et al., 1999, Carroll, et al., 2002, Chen, et al., 2008). This observation is consistent with another validation study comparing $H_2{}^{15}O$ PET and single slice ASL that reported highly consistent estimates of CBF in gray matter but less so in white matter across the two imaging platforms (Ye, et al., 2000).

Local differences in perfusion detected with ASL have successfully differentiated frontotemporal and Alzheimer-type dementias from each other and from healthy individuals (Du, et al., 2006), distinguished tumor types on the basis of vascular density (Noguchi, et al., 2008), and identified the epileptogenic hemisphere in patients with temporal lobe epilepsy (Wolf, et al., 2001). ASL has also been useful in evaluating baseline perfusion effects on function (Lee, et al., 2009) and in fMRI blood-oxygenation level dependent (BOLD) differences in health (Fernandez-Seara, et al., 2007; Zou, et al., 2009), aging (Lee, et al., 2009), and neuropsychiatric conditions (Gazdzinski, et al., 2006; Clark, et al., 2007).

Current methods enabling whole-brain coverage during perfusion scanning (Wong, et al., 1998) have the potential of providing precise CBF profiles of sparing and compromise of specific neural circuitry nodes, especially when merged with high-resolution, parcellated structural MRI data. Merging CBF data with co-registered high resolution parcellation data allows for unbiased evaluation of CBF in regions defined on structural images rather than on the CBF images themselves, thus avoiding using the dependent variable to define itself. Such regional information could enable differential diagnosis of dementias, for example, and tracking of trajectories of progressive conditions with and without treatment interventions. Establishment of normal patterns of regional CBF of specific gray matter structures across the full extent of the brain and patterns of hemispheric laterality would be critical for interpreting activated and resting state functional MRI data that depend on perfusion capacity for producing the BOLD effect (Raichle, et al., 2001; Greicius, et al., 2003; Raichle and Snyder, 2007) as well as enabling accurate interpretation of neurological conditions with lateralized pathology, such as epilepsy.

A few ASL reliability studies have been conducted on single-slice acquisition (Ye, et al., 2000) and multi-slice protocols (Grandin, et al., 2005). One repeatability study used a multi-slice continuous ASL procedure to examine global and regional CBF gray matter maps based on anterior, middle, and posterior arterial distributions (Floyd, et al., 2003). Two sets of normal volunteers were scanned twice: one pair of scans was acquired with a 1-hour

interval and the other with a 1-week interval. The within-subject coefficients of variation (wsCV) with the short interval were ~6% for whole brain CBF and ~13% for regional CBF; with a long interval, the whole brain and regional CBF were both ~14% and the difference was attributed more to variation in physiology over time and less to measurement error. Nonetheless, the relative distribution of CBF in various parts of the brain has been demonstrated to be consistent from day to day in the resting state (e.g., Aguirre, et al., 2002; Wang, et al., 2003; Parkes, et al., 2004; MacIntosh, et al.; 2008, Xu, et al.; 2009, Petersen, et al., 2010).

Pulsed continuous ASL (PCASL) employs rapidly repeated gradient and radio frequency (RF) pulses to achieve continuous labeling with high efficiency (Dai, et al., 2008). Here we characterize the regional distribution and laterality of CBF and tested the reliability of volumetric PCASL measurements of CBF in 33 cortical, subcortical, and cerebellar regions of interest (ROIs) with gray matter segmentation. Given the recently described differentiation of projection distributions from the anatomically heterogeneous precuneus (Margulies, et al., 2009), we also measured perfusion in three sub-parcellated regions of this structure.

2. Methods

2.1. Subjects

The subjects were 4 men and 6 women, age 23 to 66 years (34.8±12.5 years). All were highly educated (college graduates or beyond), and none smoked cigarettes; all but one man were right handed as determined by quantitative testing (Crovitz and Zener, 1962). Subjects were scanned twice, separated by 3 to 7 days (mean=5.8 days), and none was permitted to have caffeinated beverages within an hour of either scanning session. Whether eyes were open or closed during scanning was not controlled.

2.2. Image Acquisition

Data were collected on a GE 3T Signa Excite human whole-body system with a receive-only 8-channel array head coil and body transmit coil. The image acquisition protocol comprised a whole-brain PCASL (Wu, et al., 2007) 3D perfusion sequence (Dai, et al., 2008) (TR=5.5 s, TE=5.2 ms, thick=5 mm, skip=0 mm, xy matrix=518 × 8 (spiral acquisition); flip angle=155°, locations=36, FOV=240 mm, labeling duration=1.5 s, post labeling delay=2 s; imaging time ~6 min) (Figure 1).

Accompanying structural data were acquired with SPoiled Gradient Recall (SPGR) (TR=5.916 ms, TE=1.92 ms, thick=1.3 mm, skip=0 mm, xy matrix=256; flip angle=15°, locations=124, FOV=240 mm) and dual-echo fast spin echo (FSE) (TR=5000 ms, TE=12.248/97.984 ms, thick=2.5 mm, skip=0 mm, xy matrix=256; flip angle=90°, locations=72, FOV=240 mm) sequences.

Regridding was performed on a 256 × 256 matrix with approximately twice the Nyquist sampling density required by the field of view and twice the extent in k-space required by the actual k-space coverage. After Fourier transformation, the center 128 × 128 matrix of the image, corresponding to the prescribed field of view, was extracted. The nominal resolution of this image, 1.9 mm, is smaller than the actual resolution, estimated from the applied gradient trajectories to be 3.6 mm.

2.3. CBF Quantification

Following the method of Jarnum and colleagues (Jarnum, et al., 2009), ASL quantification was based on a two-compartment model (Alsop and Detre, 1996) with finite labeling duration (Wang, et al., 2005). Calculation of flow was based on the following equation:

$$f = \frac{\lambda}{2\alpha T_{1b}\left(1 - e^{-\frac{\tau}{T_{1b}}}\right)} \frac{(S_{ctrl} - S_{lbl})\left(1 - e^{-\frac{t_{sat}}{T_{1g}}}\right)}{S_{ref}} e^{\frac{w}{T_{1b}}}$$

where f is the flow; S is the signal from the control, label, or reference image as determined by the subscript; $T1_b$ is the T1 of blood; $T1_g$ is the T1 of gray matter; α is the labelling efficiency; λ is the brain-blood partition coefficient; τ is the labelling duration (1.5s); and *w* is the post-labelling delay. The assumed parameters were 1.2 s for $T1_g$ and 1.6 s for $T1_b$, 0.6 for effective labelling efficiency (Garcia, et al., 2005, Dai, et al., 2008), and 0.9 for the brain-blood partition coefficient (Herscovitch and Raichle, 1985). The quantification was implemented using the Interactive Data Language (IDL, Boulder, CO).

2.4. Image Processing

For each subject, an intensity bias field correction was first applied to the SPGR and FSE images (Likar, et al., 2001). The bias-corrected early-echo images were then aligned with the bias-corrected SPGR images via nonrigid registration (Rueckert, et al., 1999; Rohlfing and Maurer, 2003). The early-echo and late-echo FSE images were acquired in perfect alignment, so that the early-echo-to-SPGR alignment also applied to the late-echo FSE image. Skull-stripped images were generated by running the FSL Brain Extraction Tool (BET) (Smith, 2002) on the SPGR, early-echo, and late-echo FSE images separately and combining the resulting brain masks by voting (Rohlfing and Maurer, 2005) after reformatting the two FSE masks into SPGR space. The skull-stripped SPGR images were then segmented into three tissue classes (gray matter, white matter, and cerebrospinal fluid [CSF]) using FSL FAST (Zhang, et al., 2001).

For each subject and each acquisition session, the CBF images were aligned with the gray-matter probability maps obtained using FAST from the time 1 SPGR images. The rationale behind this procedure is that CBF signal is expected to be predominantly in gray matter. We also evaluated other possible registration protocols using proton density-weighted images acquired in alignment with the CBF images as part of the ASL acquisition protocol. The tissue contrast and conspicuity of these auxiliary images were poor by visual inspection and resulted in unreliable and inaccurate registrations. Further, assessment of CBF across the entire gray matter compartment was 2 to 3% higher for the registration via the gray-matter probability maps than via the proton density-weighted images (paired t-test, p=.0001 for time 1 and 2).

For ROI-based analysis and inter-subject comparison, we registered all skull-stripped subject SPGR images to the SPGR channel of the SRI24 atlas (Rohlfing, et al., 2008, 2010) (http://nitrc.org/projects/sri24/). Using these transformations, ROIs defined in the atlas were transferred to each subject's SPGR image space. The SRI24 atlas parcellation scheme, adapted from Tzourio-Mazoyer et al. (Tzourio-Mazoyer, et al., 2002), was collapsed into 16 bilateral ROIs and a midline cerebellar vermis ROI (Table 1, Figure 2). Also, via concatenation of SRI24-to-subject with subject SPGR-to-subject CBF images, all CBF images were reformatted into SRI24 coordinate space for averaging and visualization.

Using the segmentation maps in each subject's native space, data were analyzed as CBF in ml/100 cc of gray matter/min. for the cortical regions and total tissue for subcortical (hippocampus-amygdala, caudate-putamen, globus pallidus, and thalamus) and all cerebellar regions. The CBF data were corrected for inter-individual variations using two different methods: First, they were expressed as globally normalized data by dividing the CBF value of each voxel minus the mean of the whole brain CBF (gray matter+white matter+CSF) by the standard deviation of the whole brain CBF [(voxel CBF − whole brain mean CBF)/ whole brain CBF SD)] and also as ratios of each ROI CBF to the total brain CBF.

3. Results

3.1. Regional Distribution

The average (uncorrected) total cortical CBF was 39.5 ml/100 cc of gray matter/min. CBF differed by almost two-fold across the cortical ROIs, with the posterior cingulate cortex having the highest values. In general, cortical and cerebellar CBF was greater than subcortical CBF. Among the subcortical gray matter structures, the globus pallidus had the lowest measured CBF. The rank ordering of the native CBF all 33 ROIs was essentially the same from time 1 to time 2 (Fig. 3 and 4).

3.2. Lateral Asymmetry

Lateral asymmetry, tested with paired t-tests on globally normalized data, revealed significant ($p \leq .01$) laterality effects, with frontal regions having greater right than left and posterior regions having greater left than right perfusion (Fig. 5). This pattern of asymmetry was essentially the same at times 1 and 2 (p-values range from .01 to .0001).

The ratio method produced a similar pattern of asymmetry at both ASL sessions as the normalization method. Perfusion ratios were significantly ($p \leq .01$) higher in the right than left hemisphere in the lateral and medial frontal ROIs, whereas the left was higher than the right in the precuneus, parietal, occipital, calcarine, and superior cerebellar ROIs. At the second ASL session, the right-greater-than-left difference was not significant for the medial frontal ROI (p=.082). The advantage of the regression normalization approach is that the resultant data are normally distributed and can be expressed as effect sizes.

3.3. Parcellated Precuneus

Given the heterogeneity of perfusion levels within the precuneus and recently described differentiation of projection distributions from this anatomically heterogeneous structure (Margulies, et al., 2009), in each hemisphere we measured perfusion in three sub-parcellated regions: anterior, central, and posterior. The regional perfusion was graded, being highest in the central and posterior precuneus and lowest in the anterior precuneus, although all six sub-parcellations were greater than the cortical average. As with the total precuneus, perfusion was significantly greater in the left than right hemisphere in all three of its divisions (Fig. 6) at both scans (p-values range from .012 to .0006).

3.4. Reliability

The average uncorrected cortical CBF was 39.5±5.7 SD at time 1 and 39.8±6.6 SD ml/100 cc of gray matter/min. at time 2. Despite the similar means, the average uncorrected cortical CBF at time 2 ranged from 20% lower to 41% higher than at time 1, with 5 subjects being higher and 5 lower. The one subject with the greatest time 1–2 discrepancy was run a third time, which resulted in a difference of only 5% from the initial scan. The correlation between global uncorrected CBF at time 1 compared with time 2 was r=.36, p=.311. Using the data from the third rather than second scan for the outlying subject, the correlation was r=.60, p=.067.

Test-retest reliability was estimated by correlating the 33 ROI measures (using the total precuneus) across the 10 subjects for time 1 vs. time 2 (330 paired observations). For both approaches, the coefficient of determination was high (r^2=.924 globally normalized and r^2=.920 ratio) as was the intraclass correlation (ICC=.961 globally normalized and ICC=.957 ratio) (Fig. 7).

4. Discussion

Cerebral perfusion rates varied by two-fold across all 39 regions measured (that is, 33 plus the six sub-parcellated precuneus regions), with the posterior cingulate and posterior and central precuneus cortices having the highest perfusion and the globus pallidus the lowest. Hemispheric asymmetry in perfusion showed a consistent pattern: frontal regions had higher right than left perfusion, whereas posterior regions showed the opposite laterality effect, with left greater than right. In the aggregate the normalized regional perfusion values and hemispheric asymmetries in CBF were highly reliable when measured on separate days, whereas uncorrected global cerebral perfusion varied considerably across individuals and across sessions within an individual.

Knowledge of the normal regional variation and lateral asymmetry of cerebral blood flow is critical for interpreting apparent abnormalities in clinical settings, for example, determining location and evolution of stroke (Noguchi, et al., 2008), in localizing epileptogenic foci (Wolf, et al., 2001), examining the effects of substance abuse and smoking (Gazdzinski, et al., 2006; Clark, et al., 2007), and for differential diagnosis of dementias (Du, et al., 2006), and in assessing extent, loci, and outcome of brain injury, regardless of etiology.

Reasons for the lack of repeatability of global perfusion rates can be due to many factors including variation in cardiovascular status. For instance, the subject with the greatest inter-scan discrepancy was a professional bicycle rider with an exceedingly low resting heart rate and who was tested at mid-day for the two similar values and earlier in the morning for the aberrant value. Simultaneous acquisition of pulse and respiration rate, and potentially other measurable factors such as end tidal CO_2 and hematocrit before or even during scanning might provide additional data for adjusting global perfusion values.

The use of the higher, 3 Tesla, field for our study provides signal-to-noise advantages, but it also has the potential to amplify other sources of error (Golay, et al., 2005; Golay and Petersen, 2006). In particular, non-uniformities of the radiofrequency transmit and receive fields and the static magnetic field are greater at higher field. Our sequence employed adiabatic labeling and background suppression pulses, a fast spin echo acquisition, and a quantification approach based on a separate reference image to reduce the contribution of these error sources. Test-retest comparisons across field strength are a potential interesting future direction to better understand the contribution of these effects to reproducibility.

Left-right lateral asymmetry appears to be a normal attribute of cerebral perfusion, not dissimilar to structural asymmetry. A study using the Xenon technique reported similar perfusion asymmetry, especially with left greater than right posterior cortical CBF (Rodriguez, et al., 1991). Similarly, an ASL study that segmented the brain into distributions of the vascular territories of the three main cerebral arteries did not statistically test laterality, but inspection of the tables indicates greater left than right perfusion for the anterior cerebral artery territory (Floyd, et al., 2003). The middle branches of the anterior cerebral artery supply the cingulate gyrus and the posterior branches supply the precuneus (refer to page 637 in Gray, 1964).

The observed low CBF in the basal ganglia may be due to the short arterial transit time to the basal ganglia allowing the spins to move from the blood pool into tissue sooner than they

do in the cortex. Additionally, in the globus pallidus the spins are exposed to the presence of a substantial amount of iron, resulting in further T1 shortening (Hallgren and Sourander, 1958, Bartzokis, et al., 2008, Pfefferbaum, et al., 2009) and lower apparent CBF values. Concurrently acquired relaxivity data and PCASL scans in subjects across a substantial age range, wherein regional iron concentration varies significantly, could establish the contribution of T1 shortening to local PCASL values.

The posterior cingulate cortex and the recently described differentiation of projection distributions of the posterior portion of the anatomically heterogeneous precuneus (Margulies, et al., 2009) are sites of high intrinsic task-free functional brain activity in nodes of the "default mode network" (Raichle, et al., 2001). These anatomical sites also have the greatest cerebral blood flow.

Acknowledgments

References

Aguirre GK, Detre JA, Zarahn E, Alsop DC. Experimental design and the relative sensitivity of BOLD and perfusion fMRI. NeuroImage. 2002; 15:488–500. [PubMed: 11848692]

Alsop DC, Detre JA. Reduced transit-time sensitivity in noninvasive magnetic resonance imaging of human cerebral blood flow. Journal of Cerebral Blood Flow & Metabolism. 1996; 16:1236–1249. [PubMed: 8898697]

Barbier EL, Lamalle L, Decorps M. Methodology of brain perfusion imaging. J Magnetic Resonance Imaging. 2001; 13:496–520.

Bartzokis G, Lu PH, Tingus K, Mendez MF, Richard A, Peters DG, Oluwadara B, Barrall KA, Finn JP, Villablanca P, Thompson PM, Mintz J. Lifespan trajectory of myelin integrity and maximum motor speed. Neurobiology of Aging. 2008 Epub October 15, ahead of print.

Campbell AM, Beaulieu C. Comparison of multislice and single-slice acquisitions for pulsed arterial spin labeling measurements of cerebral perfusion. Magn Reson Imaging. 2006; 24:869–876. [PubMed: 16916704]

Carroll TJ, Teneggi V, Jobin M, Squassante L, Treyer V, Hany TF, Burger C, Wang L, Bye A, Von Schulthess GK, Buck A. Absolute quantification of cerebral blood flow with magnetic resonance, reproducibility of the method, and comparison with H2(15)O positron emission tomography. Journal of Cerebral Blood Flow & Metabolism. 2002; 22:1149–1156. [PubMed: 12218421]

Chen JJ, Wieckowska M, Meyer E, Pike GB. Cerebral Blood Flow Measurement Using fMRI and PET: A Cross-Validation Study. International Journal of Biomedical Imaging. 2008; 2008:516359. [PubMed: 18825270]

Clark CP, Brown GG, Eyler LT, Drummond SP, Braun DR, Tapert SF. Decreased perfusion in young alcohol-dependent women as compared with age-matched controls. American Journal of Drug and Alcohol Abuse. 2007; 33:13–19. [PubMed: 17366242]

Crovitz HF, Zener KA. Group test for assessing hand and eye dominance. American Journal of Psychology. 1962; 75:271–276. [PubMed: 13882420]

Dai W, Garcia D, de Bazelaire C, Alsop DC. Continuous flow-driven inversion for arterial spin labeling using pulsed radio frequency and gradient fields. Magnetic Resonance in Medicine. 2008; 60:1488–1497. [PubMed: 19025913]

Detre JA, Leigh JS, Williams DS, Koretsky AP. Perfusion imaging. Magnetic Resonance in Medicine. 1992; 23:37–45. [PubMed: 1734182]

Du AT, Jahng GH, Hayasaka S, Kramer JH, Rosen HJ, Gorno-Tempini ML, Rankin KP, Miller BL, Weiner MW, Schuff N. Hypoperfusion in frontotemporal dementia and Alzheimer disease by arterial spin labeling MRI. Neurology. 2006; 67:1215–1220. [PubMed: 17030755]

Ernst T, Chang L, Itti L, Speck O. Correlation of regional cerebral blood flow from perfusion MRI and spect in normal subjects. Magnetic Resonance Imaging. 1999; 17:349–354. [PubMed: 10195577]

Fernandez-Seara MA, Wang J, Wang Z, Korczykowski M, Guenther M, Feinberg DA, Detre JA. Imaging mesial temporal lobe activation during scene encoding: comparison of fMRI using BOLD and arterial spin labeling. Human Brain Mapping. 2007; 28:1391–1400. [PubMed: 17525983]

Floyd TF, Ratcliffe SJ, Wang J, Resch B, Detre JA. Precision of the CASL-perfusion MRI technique for the measurement of cerebral blood flow in whole brain and vascular territories. Journal of Magnetic Resonance in Imaging. 2003; 18:649–655.

Garcia DM, Duhamel G, Alsop DC. Efficiency of inversion pulses for background suppressed arterial spin labeling. Magnetic Resonance in Medicine. 2005; 54:366–372. [PubMed: 16032674]

Gazdzinski S, Durazzo T, Jahng GH, Ezekiel F, Banys P, Meyerhoff D. Effects of chronic alcohol dependence and chronic cigarette smoking on cerebral perfusion: a preliminary magnetic resonance study. Alcoholism: Clinical and Experimental Research. 2006; 30:947–958.

Golay X, Petersen ET. Arterial spin labeling: benefits and pitfalls of high magnetic field. Neuroimaging Clinics of North America. 2006; 16:259–268. [PubMed: 16731365]

Golay X, Petersen ET, Hui F. Pulsed star labeling of arterial regions (PULSAR): a robust regional perfusion technique for high field imaging. Magnetic Resonance in Medicine. 2005; 53:15–21. [PubMed: 15690497]

Grandin CB, Bol A, Smith AM, Michel C, Cosnard G. Absolute CBF and CBV measurements by MRI bolus tracking before and after acetazolamide challenge: repeatabilily and comparison with PET in humans. NeuroImage. 2005; 26:525–535. [PubMed: 15907309]

Gray, H. Anatomy of the Human Body. Lea & Febiger; Philadelphia: 1964.

Greicius MD, Krasnow B, Reiss AL, Menon V. Functional connectivity in the resting brain: a network analysis of the default mode hypothesis. Proceedings of the National Academy of Sciences of the United States of America. 2003; 100:253–258. [PubMed: 12506194]

Hallgren B, Sourander P. The effect of age on the non-haemin iron in the human brain. Journal of Neurochemistry. 1958; 3:41–51. [PubMed: 13611557]

Herscovitch P, Raichle ME. What is the correct value for the brain--blood partition coefficient for water? Journal of Cerebral Blood Flow & Metabolism. 1985; 5:65–69. [PubMed: 3871783]

Jarnum H, Steffensen EG, Knutsson L, Frund ET, Simonsen CW, Lundbye-Christensen S, Shankaranarayanan A, Alsop DC, Jensen FT, Larsson EM. Perfusion MRI of brain tumours: a comparative study of pseudo-continuous arterial spin labelling and dynamic susceptibility contrast imaging. Neuroradiology. 2009

Lee C, Lopez OL, Becker JT, Raji C, Dai W, Kuller LH, Gach HM. Imaging cerebral blood flow in the cognitively normal aging brain with arterial spin labeling: implications for imaging of neurodegenerative disease. Journal of Neuroimaging. 2009; 19:344–352. [PubMed: 19292827]

Likar B, Viergever MA, Pernus F. Retrospective correction of MR intensity inhomogeneity by information minimization. EEE Transactions on Medical Imaging. 2001; 20:1398–1410.

MacIntosh BJ, Pattinson KT, Gallichan D, Ahmad I, Miller KL, Feinberg DA, Wise RG, Jezzard P. Measuring the effects of remifentanil on cerebral blood flow and arterial arrival time using 3D GRASE MRI with pulsed arterial spin labelling. Journal of Cerebral Blood Flow & Metabolism. 2008; 28:1514–1522. [PubMed: 18506198]

Margulies DS, Vincent JL, Kelly C, Lohmann G, Uddin LQ, Biswal BB, Villringer A, Castellanos FX, Milham MP, Petrides M. Precuneus shares intrinsic functional architecture in humans and monkeys. Proceedings of the National Academy of Sciences of the United States of America. 2009; 106:20069–20074. [PubMed: 19903877]

Noguchi T, Yoshiura T, Hiwatashi A, Togao O, Yamashita K, Nagao E, Shono T, Mizoguchi M, Nagata S, Sasaki T, Suzuki SO, Iwaki T, Kobayashi K, Mihara F, Honda H. Perfusion imaging of brain tumors using arterial spin-labeling: correlation with histopathologic vascular density. AJNR American Journal of Neuroradiology. 2008; 29:688–693. [PubMed: 18184842]

Parkes LM, Rashid W, Chard DT, Tofts PS. Normal cerebral perfusion measurements using arterial spin labeling: reproducibility, stability, and age and gender effects. Magnetic Resonance in Medicine. 2004; 51:736–743. [PubMed: 15065246]

Petersen ET, Mouridsen K, Golay X. The QUASAR reproducibility study, Part II: Results from a multi-center Arterial Spin Labeling test-retest study. NeuroImage. 2010; 49:104–113. [PubMed: 19660557]

Pfefferbaum A, Adalsteinsson E, Rohlfing T, Sullivan EV. Diffusion tensor imaging of deep gray matter brain structures: Effects of age and iron concentration. Neurobiology of Aging. 2009; 31:482–493. [PubMed: 18513834]

Raichle M, MacLeod A, Snyder A, Powers W, Gusnard D, Shulman G. A default mode of brain function. Proceedings of the National Academy of Sciences of the United States of America. 2001; 98:676–682. [PubMed: 11209064]

Raichle ME, Snyder AZ. A default mode of brain function: a brief history of an evolving idea. NeuroImage. 2007; 37:1083–1090. discussion 1097–1089. [PubMed: 17719799]

Rodriguez G, Coppola R, De Carli F, Francione S, Marenco S, Nobili F, Risberg J, Rosadini G, Warkentin S. Regional cerebral blood flow asymmetries in a group of 189 normal subjects at rest. Brain Topography. 1991; 4:57–63. [PubMed: 1764351]

Rohlfing T, Maurer CR. Nonrigid image registration in shared-memory multiprocessor environments with application to brains, breasts, and bees. IEEE Transactions on Information Technology in Biomedicine. 2003; 7:16–25. [PubMed: 12670015]

Rohlfing T, Maurer JCR. Multi-classifier framework for atlas-based image segmentation. Pattern Recognition Letters. 2005; 26:2070–2079.

Rohlfing, T.; Zahr, NM.; Sullivan, EV.; Pfefferbaum, A. The SRI24 multi-channel brain atlas: Construction and applications Medical Imaging 2008: Image Processing. Proceedings of SPIE 6914, EID 691409; 2008. (691412 pages)

Rohlfing T, Zahr NM, Sullivan EV, Pfefferbaum A. The SRI24 multi-channel atlas of normal adult human brain structure. Human Brain Mapping. 2010 in press.

Rueckert D, Sonoda LI, Hayes C, Hill DL, Leach MO, Hawkes DJ. Nonrigid registration using free-form deformations: application to breast MR images. IEEE Transactions on Medical Imaging. 1999; 18:712–721. [PubMed: 10534053]

Smith S. Fast robust automated brain extraction. Human Brain Mapping. 2002; 17:143–155. [PubMed: 12391568]

Tzourio-Mazoyer N, Landeau B, Papathanassiou D, Crivello F, Etard O, Delcroix N, Mazoyer B, Joliot M. Automated anatomical labeling of activations in SPM using a macroscopic anatomical parcellation of the MNI MRI single-subject brain. NeuroImage. 2002; 15:273–289. [PubMed: 11771995]

Wang J, Aguirre GK, Kimberg DY, Roc AC, Li L, Detre JA. Arterial spin labeling perfusion fMRI with very low task frequency. Magnetic Resonance in Medicine. 2003; 49:796–802. [PubMed: 12704760]

Wang J, Zhang Y, Wolf RL, Roc AC, Alsop DC, Detre JA. Amplitude-modulated continuous arterial spin-labeling 3.0-T perfusion MR imaging with a single coil: feasibility study. Radiology. 2005; 235:218–228. [PubMed: 15716390]

Wintermark M, Sesay M, Barbier E, Borbely K, Dillon WP, Eastwood JD, Glenn TC, Grandin CB, Pedraza S, Soustiel JF, Nariai T, Zaharchuk G, Caille JM, Dousset V, Yonas H. Comparative overview of brain perfusion imaging techniques. Journal of Neuroradiology. 2005; 32:294–314.

Wolf RL, Alsop DC, Levy-Reis I, Meyer PT, Maldjian JA, Gonzalez-Atavales J, French JA, Alavi A, Detre JA. Detection of mesial temporal lobe hypoperfusion in patients with temporal lobe epilepsy by use of arterial spin labeled perfusion MR imaging. AJNR American Journal of Neuroradiology. 2001; 22:1334–1341. [PubMed: 11498422]

Wong EC, Buxton RB, Frank LR. A theoretical and experimental comparison of continuous and pulsed arterial spin labeling techniques for quantitative perfusion imaging. Magnetic Resonance in Medicine. 1998; 40:348–355. [PubMed: 9727936]

Wu WC, Fernandez-Seara M, Detre JA, Wehrli FW, Wang J. A theoretical and experimental investigation of the tagging efficiency of pseudocontinuous arterial spin labeling. Magnetic Resonance in Medicine. 2007; 58:1020–1027. [PubMed: 17969096]

Xu G, Rowley HA, Wu G, Alsop DC, Shankaranarayanan A, Dowling M, Christian BT, Oakes TR, Johnson SC. Reliability and precision of pseudo-continuous arterial spin labeling perfusion MRI

on 3.0 T and comparison with (15)O-water PET in elderly subjects at risk for Alzheimer's disease. NMR in Biomedicine. 2009 Epub December 1, ahead of print.

Ye FQ, Berman KF, Ellmore T, Esposito G, van Horn JD, Yang Y, Duyn J, Smith AM, Frank JA, Weinberger DR, McLaughlin AC. H(2)(15)O PET validation of steady-state arterial spin tagging cerebral blood flow measurements in humans. Magnetic Resonance in Medicine. 2000; 44:450–456. [PubMed: 10975898]

Zhang Y, Brady M, Smith S. Segmentation of brain MR images through a hidden Markov random field model and the expectation maximization algorithm. IEEE Transactions Medical Imaging. 2001; 20:45–57.

Zou Q, Wu CW, Stein EA, Zang Y, Yang Y. Static and dynamic characteristics of cerebral blood flow during the resting state. NeuroImage. 2009; 48:515–524. [PubMed: 19607928]
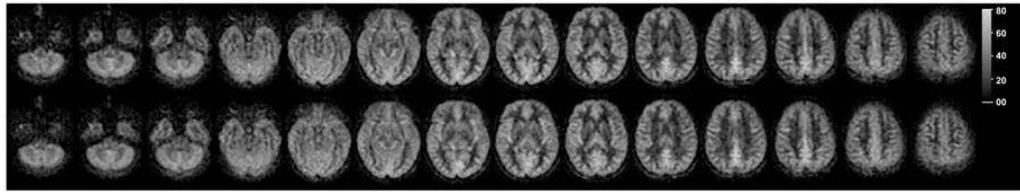
Figure 1.
CBF images from a 28 year-old woman. Top: first scan. Bottom: second scan 6 days later. The intensity scale is in units of ml/100cc of gray matter/min.
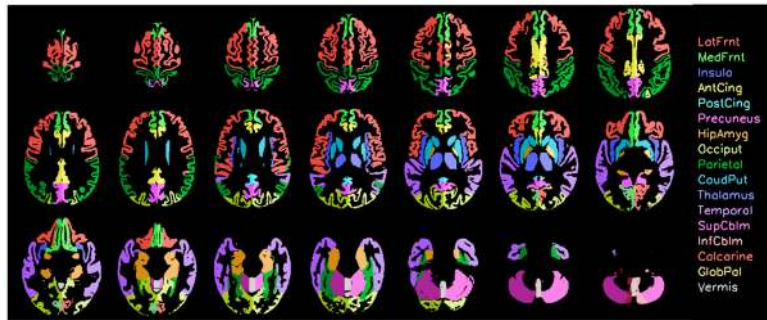
Figure 2.
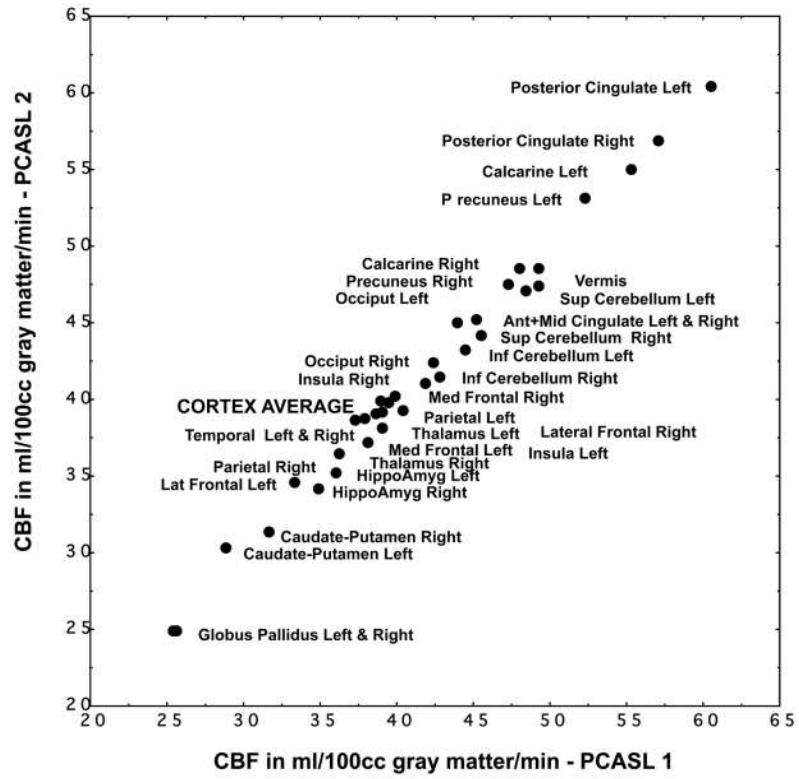33 color-coded gray matter or tissue-segmented regions of interest (ROIs) used to assess CBF.

Figure 3.
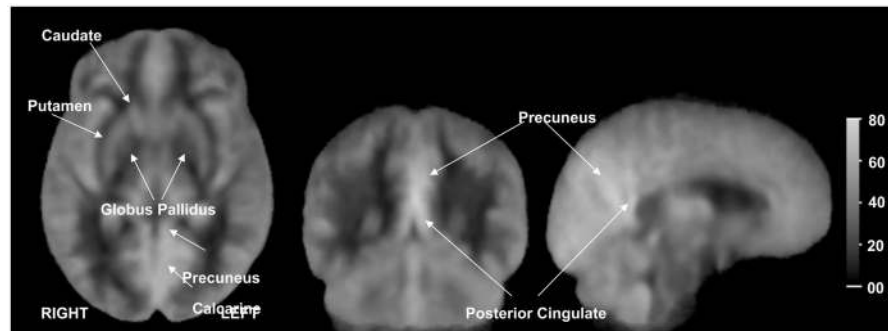CBF for 33 ROIs for PCASL time 1 compared with PCASL time 2.

Figure 4.
Group average axial, coronal, and sagittal CBF images, noted regions of high (precuneus, posterior cingulate, and calcarine cortices), low (caudate and putamen), and even lower (globus pallidus) perfusion. The intensity scale is in units of ml/100cc of gray matter/min.
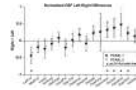
Figure 5.
CBF left-right differences (means ± standard deviations) for 16 bilateral normalized ROIs. PCASL 1 = black, PCASL 2 = gray. Below 0 = right greater than left. Above 0 = left greater than right.
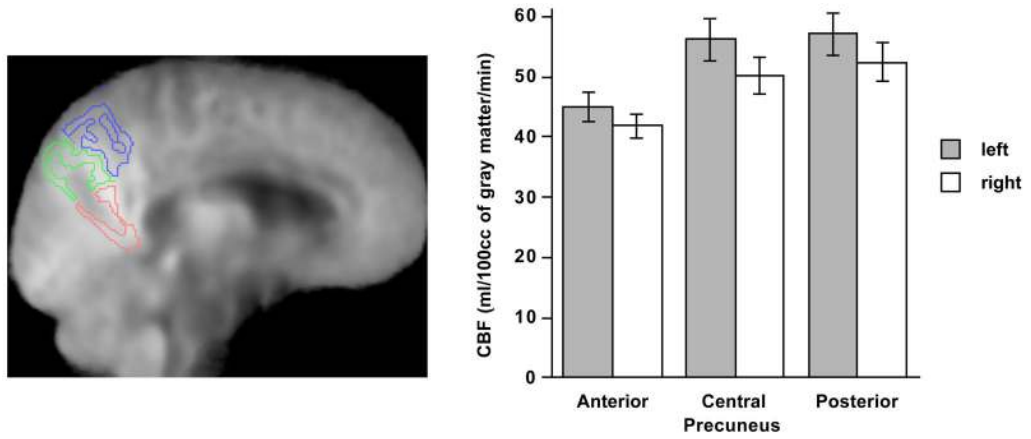
Figure 6.
Precuneus subdivided into anterior (blue), central (green) and posterior (red) gray matter ROIs superimposed on a left parasagittal group average CBF image (left). Mean±standard error CBF from PCASL 1 of the three bilateral precuneus subsegments (right).

Figure 7.
Globally normalized CBF for each of the 33 ROIs for each subject (n=330 observations) for
PCASL 1 plotted against PCASL 2.

Table 1

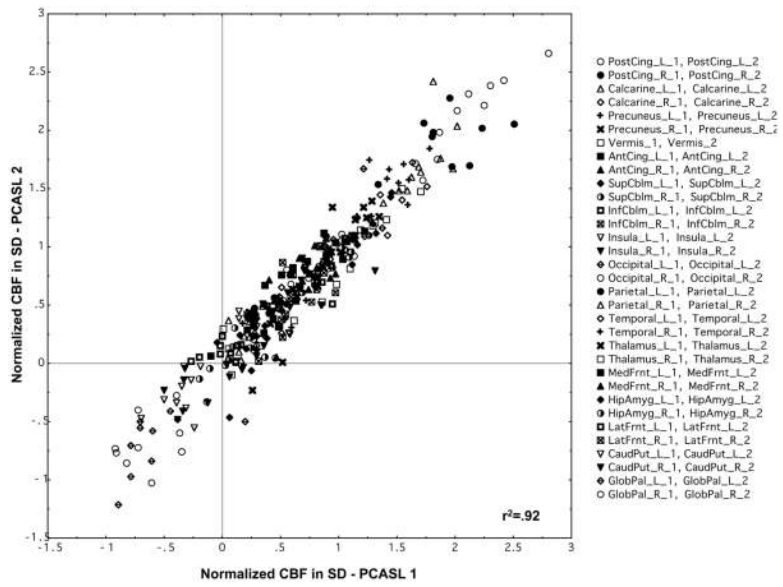| ASL_ROI	Left			Right		
	Tzourio-Mazoyer name	SRI24 code	Tzourio-Mazoyer code	Tzourio-Mazoyer name	SRI24 code	Tzourio-Mazoyer code
Lateral Frontal	Precentral_L	1	2001	Precentral_R	2	2002
Lateral Frontal	Frontal_Sup_L	3	2101	Frontal_Sup_R	4	2102
Lateral Frontal	Frontal_Sup_Orb_L	5	2111	Frontal_Sup_Orb_R	6	2112
Lateral Frontal	Frontal_Mid_L	7	2201	Frontal_Mid_R	8	2202
Lateral Frontal	Frontal_Mid_Orb_L	9	2211	Frontal_Mid_Orb_R	10	2212
Lateral Frontal	Frontal_Inf_Oper_L	11	2301	Frontal_Inf_Oper_R	12	2302
Lateral Frontal	Frontal_Inf_Tri_L	13	2311	Frontal_Inf_Tri_R	14	2312
Lateral Frontal	Frontal_Inf_Orb_L	15	2321	Frontal_Inf_Orb_R	16	2322
Lateral Frontal	Rolandic_Oper_L	17	2331	Rolandic_Oper_R	18	2332
Lateral Frontal	Supp_Motor_Area_L	19	2401	Supp_Motor_Area_R	20	2402
Medial Frontal	Olfactory_L	21	2501	Olfactory_R	22	2502
Medial Frontal	Frontal_Sup_Medial_L	23	2601	Frontal_Sup_Medial_R	24	2602
Medial Frontal	Frontal_Med_Orb_L	25	2611	Frontal_Med_Orb_R	26	2612
Medial Frontal	Rectus_L	27	2701	Rectus_R	28	2702
Insula	Insula_L	29	3001	Insula_R	30	3002
Cingulum_Ant+Mid	Cingulum_Ant_L	31	4001	Cingulum_Ant_R	32	4002
Cingulum_Ant+Mid	Cingulum_Mid_L	33	4011	Cingulum_Mid_R	34	4012
Cingulum_Post	Cingulum_Post_L	35	4021	Cingulum_Post_R	36	4022
Hippocampus+Amygdala	Hippocampus_L	37	4101	Hippocampus_R	38	4102
Hippocampus+Amygdala	ParaHippocampal_L	39	4111	ParaHippocampal_R	40	4112
Hippocampus+Amygdala	Amygdala_L	41	4201	Amygdala_R	42	4202
Calcarine	Calcarine_L	43	5001	Calcarine_R	44	5002
Occipital	Cuneus_L	45	5011	Cuneus_R	46	5012
Occipital	Lingual_L	47	5021	Lingual_R	48	5022
Occipital	Occipital_Sup_L	49	5101	Occipital_Sup_R	50	5102
Occipital	Occipital_Mid_L	51	5201	Occipital_Mid_R	52	5202
Occipital	Occipital_Inf_L	53	5301	Occipital_Inf_R	54	5302
Parietal	Fusiform_L	55	5401	Fusiform_R	56	5402

ASL_ROI	Left			Right		
	Tzourio-Mazoyer name	SR124 code	Tzourio-Mazoyer code	Tzourio-Mazoyer name	SR124 code	Tzourio-Mazoyer code
Parietal	Postcentral_L	57	6001	Postcentral_R	58	6002
Parietal	Parietal_Sup_L	59	6101	Parietal_Sup_R	60	6102
Parietal	Parietal_Inf_L	61	6201	Parietal_Inf_R	62	6202
Parietal	SupraMarginal_L	63	6211	SupraMarginal_R	64	6212
Parietal	Angular_L	65	6221	Angular_R	66	6222
Parietal	Paracentral_Lobule_L	69	6401	Paracentral_Lobule_R	70	6402
Precuneus	Precuneus_L	67	6301	Precuneus_R	68	6302
Caudate+Putamen	Caudate_L	71	7001	Caudate_R	72	7002
Caudate+Putamen	Putamen_L	73	7011	Putamen_R	74	7012
Globus Pallidus	Pallidum_L	75	7021	Pallidum_R	76	7022
Thalamus	Thalamus_L	77	7101	Thalamus_R	78	7102
Temporal	Heschl_L	79	8101	Heschl_R	80	8102
Temporal	Temporal_Sup_L	81	8111	Temporal_Sup_R	82	8112
Temporal	Temporal_Pole_Sup_L	83	8121	Temporal_Pole_Sup_R	84	8122
Temporal	Temporal_Mid_L	85	8201	Temporal_Mid_R	86	8202
Temporal	Temporal_Pole_Mid_L	87	8211	Temporal_Pole_Mid_R	88	8212
Temporal	Temporal_Inf_L	89	8301	Temporal_Inf_R	90	8302
Cerebellum_Superior	Cerebellum_Crus1_L	91	9001	Cerebellum_Crus1_R	92	9002
Cerebellum_Superior	Cerebellum_3_L	95	9021	Cerebellum_3_R	96	9022
Cerebellum_Superior	Cerebellum_4_5_L	97	9031	Cerebellum_4_5_R	98	9032
Cerebellum_Superior	Cerebellum_6_L	99	9041	Cerebellum_6_R	100	9042
Cerebellum_Inferior	Cerebellum_Crus2_L	93	9011	Cerebellum_Crus2_R	94	9012
Cerebellum_Inferior	Cerebellum_7b_L	101	9051	Cerebellum_7b_R	102	9052
Cerebellum_Inferior	Cerebellum_8_L	103	9061	Cerebellum_8_R	104	9062
Cerebellum_Inferior	Cblm_Tonsil_9_L	105	9071	Cblm_Tonsil_9_R	106	9072
Cerebellum_Inferior	Cerebelum_10_L	107	9081	Cerebelum_10_R	108	9082
Vermis	Vermis_1	128	9100			
Vermis	Vermis_2	129	9110			
Vermis	Vermis_3	130	9120			